Development of a 6-Degrees-of-Freedom Hybrid Interface Intended for Teleoperated Robotic Cervical Spine Surgery

Alizée Koszulinski, Juan Sandoval, Marc Arsicault, Med Amine Laribi

Development of a 6 degrees-of-freedom hybrid interface intended for teleoperated robotic cervical spine surgery

Alizée Koszulinski[1]
Department GMSC – Pprime Institute, CNRS – University of Poitiers – ENSMA,
Poitiers 86073, France
e-mail: alizee.koszulinski@univ-poitiers.fr

Juan Sandoval
Nantes Université, École Centrale Nantes, CNRS, LS2N, UMR 6004,
Nantes 44000, France
e-mail: juan.sandoval@ls2n.fr

Marc Arsicault
Department GMSC – Pprime Institute, CNRS – University of Poitiers – ENSMA,
Poitiers 86073, France
e-mail: marc.arsicault@univ-poitiers.fr

Med Amine Laribi
Department GMSC – Pprime Institute, CNRS – University of Poitiers – ENSMA,
Poitiers 86073, France
e-mail: med.amine.laribi@univ-poitiers.fr
ASME Member

ABSTRACT

This paper deals with the development of a 6-degrees-of-freedom (DoF) hybrid interface for a teleoperated robotic platform intended to assist surgeons in cervical spine surgery. The targeted task is the drilling of cervical vertebrae for the attachment of spinal implants. Given the complex anatomy of the cervical region, with the proximity of the spinal cord and vertebral arteries, high accuracy in the drilling procedure is required to avoid complications for the patient. In this context, the proposed hybrid interface has been designed to meet the requirements of the drilling task, in terms of degrees of freedom, workspace and force feedback,

[1] Corresponding author.

which have been identified through a literature review. It consists of an association of two parallel mechanisms and a centrally located serial mechanism. Direct and inverse kinematic modelling of each mechanism as well as the one of the complete interface were carried out. A study of the dexterity distribution of the parallel mechanisms was carried out in order to select the suitable interface working mode that would keep the singularities away from the prescribed workspace. In addition, the force feedback was implemented in static mode, neglecting in a first time the weight of the system. The interface design parameters were then optimized to avoid singularities within the prescribed workspace, to minimize motor torques, and to reduce the size of the interface. These development stages led to the design of a motorized prototype of the hybrid interface.

Keywords: hybrid interface, force feedback, direct and inverse kinematic models, optimization, cervical spine surgery.

1. INTRODUCTION

The orthopaedic surgery of interest to this work is called posterior cervical arthrodesis. This surgical procedure aims to treat cervical spine instabilities, which can result from degenerative diseases or trauma. When the spinal deformity is significant or the pathology is deemed to be at an advanced stage, surgery may be recommended to relieve the patient. Arthrodesis is a surgical technique that enables at least two vertebrae to be fused together, i.e. permanently consolidated. This operation frees the nerves and/or spinal cord, where these were previously compressed, and stabilizes the spine, the aim being to maintain a normal spacing between each vertebra. To achieve this, the surgeon has to drill holes in specific areas of the vertebrae so that spinal implants can be attached. These implants generally consist of screws and fixation rods (see Fig. 1). Each drilling of a cervical vertebra must be performed along an optimal trajectory defined by the surgeon according to an entry point, a direction, a diameter and a depth [1].

Identifying this optimal trajectory requires an in-depth knowledge of the anatomy of each of the patient's vertebrae. Given the proximity of the spinal cord and vertebral arteries that supply oxygenated blood to the brain, an incorrectly positioned screw could pose significant risks to the patient. High-accuracy drilling is therefore essential to preserve all the structures and vessels adjacent to the cervical spine.

Fig. 1 Illustration of posterior cervical arthrodesis

The integration of a robotic device into this surgical procedure should improve the surgeon’s abilities, particularly in terms of accuracy when performing the drilling, as it has been observed in thoracic spine surgery [2]. Currently, the existing robotic arms used for orthopaedic surgery are developed to be controlled in a comanipulation scheme, i.e. with a direct manipulation of the robotic arm by the surgeon [3]. To our knowledge, no remote-controlled robotic platform, known as teleoperation, has been developed for orthopaedic surgery, including spine surgery. A major advantage of a teleoperation platform is that it provides a more ergonomic and comfortable sitting position for the surgeon, as opposed to standing and bending over the surgical field for several hours. In this context, teleoperation could improve surgeon’s endurance by reducing fatigue as the drilling procedure progresses. Besides enhancing comfort, the reduction in surgeon fatigue could help maintain precision of movements throughout the surgery. Consequently, the development of an interface adapted to the drilling gesture is necessary to enable the adaptation of a comanipulation platform [4] to a remote control [5].

1.1. Existing rigid-link interfaces

Rigid-link interfaces can be classified into three categories according to their kinematic chain: serial architectures with joints connected in series, parallel architectures with one or more closed kinematic chains and hybrid architectures with a combination of serial and parallel mechanisms.

Fig. 2 (a) Virtuose 6D by Haption, (b) Omega 3 parallel interface by Force Dimension, (C) MEPaM developed by Abeywardena et al. and (d) Hybrid interface developed by Meskini et al.

The Virtuose 6D interface from the company Haption (Soulge-Sur-Ouette, France) thus belongs to the class of serial interfaces (see Fig. 2a). This interface was used by Ewerton *et al.* to develop a tool for real-time correction of motor skills during calligraphy exercises [6]. On the other hand, the PHANToM Desktop serial device from SensAble Technologies (Woburn, MA) was used to develop a bone preparation simulator in the dental field [7]. Concerning parallel interfaces, the Novint Falcon developed by Novint Technologies (Albuquerque, NM) and initially intended for the entertainment industry, is currently being used at the Pprime Institute (Poitiers, France) to assist ultrasound examinations using a remotely-operated robotic platform [8]. In addition, the company Force Dimension (Nyon, Switzerland) offers a range of interfaces, called "Omega" (see Fig. 2b), particularly dedicated to the field of medical robotics. In the same field, the MEPaM ("Monash Epicyclic Parallel Manipulator") has been developed by Abeywardena *et al.* for the simulation of laparoscopic surgery (see Fig. 2c) [9].

In the category of hybrid interfaces, Delta 6 device marketed by Force Dimension or the hybrid architecture with four degrees of freedom developed by Meskini *et al.* [10] developed for laparoscopic surgery (see Fig. 2d) can be cited.

Each of the above interface classes has its own advantages and disadvantages, which may direct its use for certain applications, depending on the constraints imposed, such as accuracy, compactness of the device, or the workspace it has to cover. The main features associated with each type of architecture are summarized in Table 1 below.

Table 1 Main advantages and disadvantages of the rigid-link interface classes

1.2. Novel hybrid interface for cervical spine surgery

As mentioned previously, cervical spine surgery requires great accuracy. For an interface, the rigidity of a mechanism is a key factor to guarantee its accuracy. Furthermore, the interface should be easily adaptable to the specified workspace of the drilling task.

Considering the abovementioned advantages, a hybrid architecture was chosen for the development of our interface dedicated to cervical surgery.

The key contributions of this work can be summarized as:

(1) Development of a new 6-degrees-of-freedom hybrid architecture.

(2) Decoupling of the degree of freedom associated with the drilling axis, allowing better control of the latter.

(3) Possibility of repositioning a center of rotation (CoR).

(4) Formulation of the relationship between input forces and active joint torques tailored to the needs of a vertebra drilling task.

This paper is structured as follows: Section 2 gives the specifications associated with the procedure of vertebrae drilling regarding the workspace and force feedback. Section 3 describes the proposed hybrid architecture and details the kinematic models of each mechanism as well as the complete interface. Section 4 presents the relationship between the input forces and the active joint torques. The optimization of the design parameters of the interface is discussed in section 5, which also presents the final design of a motorized prototype. Section 5 concludes this paper.

2. DRILLING TASK SPECIFICATIONS

2.1. Prescribed workspace definition

Identifying the specificities of the surgical procedure is essential for the development and sizing of an interface adapted to the drilling gesture. For this purpose, the drilling procedure can be divided into 3 steps whose required degrees of freedom can be defined and the linked workspace evaluated.

Fig. 3 Illustration of the drilling procedure and the prescribed workspaces

The first step consists in the positioning of the surgical drill at the desired entry point thus involving the three translational DoF (see Fig. 3a). Once the tip of the drill is positioned, the surgeon must adjust the orientation of the tool to perfectly align it with the optimal drilling direction (see Fig. 2b). This second step therefore requires rotations around the $\vec{x}$ and $\vec{y}$ axes of the tool. The self-rotation, around $\vec{z}$ axis, can be neglected because it corresponds to the rotation axis of the drill. However, in the context of a robotic application, this rotation can be an advantage when avoiding singular configurations by modifying the posture of the robotic arm. The last step of the gesture is the drilling performing along the

longitudinal axis of the drill corresponding to the $\vec{z}$ axis (see Fig. 3c). In summary, the need for 6 DoF was retained to fully control a robotic arm during a drilling procedure.

Several drilling gestures were investigated to further define the workspace specifications of the interface. Insertion of articular screws, superior and inferior transarticular drilling, translaminar and pedical screw fixation were thus analysed through a literature review. These five techniques are linked to the anatomical region drilled in each vertebra during surgery. In order to quantify the drilling parameters for each type of gesture, 25 articles have been retained, corresponding to a study of almost 11,500 screw insertions [11-36]. For each article and each drilling gesture, the following data were collected: the minimum and maximum drilling depth and diameter, as well as the maximum angular amplitude of the surgical drill (see Fig. 4).

Fig. 4 Summary of the results of the literature review conducted on the drilling parameters of five different drilling gestures

Based on this data, prescribed workspaces associated with the drilling task can be defined. First, the maximum workspace of the surgical drill corresponds to a cone with an apex angle of ± 29° and a height of 52 mm (see Fig. 3b and 3c). At the vertebral level, this drilling cone must be repositioned to correct the location of the tool tip, associated with the apex of the cone, thus allowing correct alignment between the axis of the tool and the optimal direction of drilling. Accordingly, this first workspace is extended by allowing translation of the top of the drilling cone inside a cylinder with a diameter and height equal to 20 mm, i.e. more than four times the maximum diameter of a cervical screw (see Fig. 3b and 3c).

At the level of the spine, a second workspace must be considered in order to position the tip of the tool close to the desired drilling entry point and also pre-orientate the tool, knowing that the average drilling angles vary depending on the anatomical region considered. This second workspace can be represented by a displacement cube, at the center of which the orientation of the tool can be adjusted (see Fig. 3a).

2.2. Drilling interaction forces

Following the definition of the prescribed workspaces for the task of drilling the cervical vertebrae, a second literature review was carried out to evaluate the forces applied during the surgical procedure. The aim was to define the interaction forces that the interface should be able to generate in order to provide realistic force feedback to the surgeon while remotely controlling the robotic arm.

A total of 7 articles and one thesis paper were retained [37-44]. The latter present the results in terms of force feedback during the performance of more than one hundred drills on vertebrae of different types: human, bovine, porcine and ovine, whose vertebral anatomy is similar to that of humans. Like the femur or the frontal bone of the skull, vertebrae are composed of a cortical part and a spongy part. The cortical bone is the dense, rigid external layer of the bone, corresponding to the white areas on an X-ray (see Fig. 5a). Spongy or cancellous bone, on the other hand, is porous and is located mainly inside the protective envelope formed by the cortical bone.

Figure 5a shows the typical curve of the force applied along the drilling axis, which can be divided into 4 phases. The first phase consists of the tool advancing until the first contact with the vertebra (A). Next, a peak in force is felt during the drilling of the first layer of cortical bone (B). The force curve then decreases as the tool enters the cancellous bone (C).

A second peak in force is sometimes seen, which is synonymous with reaching the second layer of cortical bone (D).

In the context of developing an interface for remotely controlling a robot to perform surgery, it's therefore crucial to transmit the interaction forces between the tool and the vertebra being drilled to the surgeon. This allows the surgeon to feel in which bony part the drill is located, thus avoiding the risk of unwanted vertebral perforation and potential damage to adjacent structures such as the spinal cord or vertebral arteries.

Fig. 5 (a) Typical curve of the evolution of the force applied along the drilling axis and (b) histograms of the maximum values of force and moment found in the literature

The histograms in Fig. 5b show the maximum force and moment values found in the literature in the three directions, where $\vec{z}$ axis corresponds to the drilling axis. These results led to the definition of the maximum force limits that the interface should be able to generate, which were set at 30 N along the drilling axis, 10 N along the transverse axes and 0.5 N.m for the three directions of rotation.

3. THE PROPOSED 6 DOF HYBRID INTERFACE

3.1. Description of the architecture

Considering the specific requirements for cervical vertebral drilling, a hybrid architecture interface is proposed. It combines two parallel mechanisms and a centrally located serial mechanism. The upper mechanism, a 3-RRR (R: revolute) planar parallel mechanism, enables two translations in the mechanism plane (see Fig. 6a). The lower 3-RRR mechanism allows two in-plane translations and one rotation through its mobile platform connected to three serial chains (see Fig. 6b). Connecting the end-effectors of the two parallel mechanisms by a central rod allows three degrees of rotation and three degrees of

translation. However, the translation orthogonal to the parallel mechanisms is limited and only relies on the central rod rotational movements (see Fig. 6c). A serial mechanism, fixed to the central rod and corresponding to an helical joint, thus provides complete control of this last translation associated with the drilling axis (see Fig. 6d). The assembly of the parallel and serial mechanisms must cover the displacement cube, keeping the orientation of the central rod fixed, in relation to the prescribed workspaces previously defined (see Fig. 3). In addition, it should cover the displacement cylinder and the drilling cone, allowing for modification of the position of the central rod CoR and its orientation.

Fig. 6 Representation of the interface architecture and the degrees of freedom obtain with each mechanism: (a) the upper mechanism, (b) the lower mechanism, (c) the assembly of the two parallel mechanisms and (d) the serial mechanism

Seven actuators will be used to handle the control of the proposed hybrid interface: three for each parallel mechanism and one for the serial mechanism. The upper mechanism being controlled with three actuator and allowing two degrees of freedom has thus one degree of redundancy.

3.2. Direct and inverse kinematic models of each mechanism

3.2.1. Lower parallel mechanism

The best-known resolution method for solving the direct kinematic model (DKM) of a 3-RRR mechanism with a moving platform is the one proposed by Gosselin [45]. This method consists in considering the central part of the parallel mechanism made up of the mobile platform and the six passive revolute joints, i.e. a 3-RPR (P: prismatic) type mechanism whose prismatic links have a fixed length. Knowing the joint positions of the active revolute joint, the coordinates of the first passive revolute joint of each serial chain

258 are known. In a reference frame associated with these first passive revolute joint, the
259 coordinates of the three vertices of the mobile platform can be defined. This method leads
260 to a 6th degree polynomial whose roots correspond to the six DKM solutions. The addition
261 of an encoder on one of the passive revolute joints is then essential to identify the correct
262 solution among the six. However, since the interface is used to control a robotic device
263 online, the resolution time of this method is not compatible with a real-time application
264 [46]. To cope with this issue, another resolution method, called serial, can be implemented.
265 This serial method consists of considering only one of the three serial chains of the parallel
266 mechanism to solve the DKM. This method requires the use of two sensors on the two
267 passive revolute joints. Considering the serial chain n°1 (see Fig. 7), the coordinates of
268 point B_1 associated with the first passive revolute joint of the chain can first be calculated
269 as a function of the joint position α_1 of actuator A_1 such that:

$$\begin{cases} x_{B_1} = x_{A_1} + l_1\, cos(\alpha_1) = l_1\, cos(\alpha_1) \\ y_{B_1} = y_{A_1} + l_1\, sin(\alpha_1) = l_1\, sin(\alpha_1) \end{cases} \quad (1)$$

270 where $x_{A_1} = y_{A_1} = 0$ since point A_1 is the origin of the base reference frame R_O and l_1
271 correspond to the length of the first serial chain segment.

272

273

274 *Fig. 7 Kinematic representation of (a) the lower parallel mechanism and (b) its mobile platform*

275 Using the angle ε_1 given by the sensor, the coordinates of point C_1 can be expressed as:

$$\begin{cases} x_{C_1} = x_{B_1} + l_2 \cos(\alpha_1 + \varepsilon_1) \\ y_{C_1} = y_{B_1} + l_2 \sin(\alpha_1 + \varepsilon_1) \end{cases} \quad (2)$$

276 where l_2 represents the length of the second serial chain segment.

277 Finally, the two sensors are used to determine the position and the orientation of the mobile
278 platform defined as:

$$\begin{cases} x_{P_1} = x_{C_1} + l_3 \cos(\alpha_1 + \varepsilon_1 + \varepsilon_2 + \gamma_1) \\ y_{P_1} = y_{C_1} + l_3 \sin(\alpha_1 + \varepsilon_1 + \varepsilon_2 + \gamma_1) \\ \phi_z = \text{atan2}\left(y_{C_2} - y_{C_1}, x_{C_2} - x_{C_1}\right) \end{cases} \quad (3)$$

279 with $x_{C_2} = x_{C_1} + \sqrt{3} l_3 \cos(\alpha_1 + \varepsilon_1 + \varepsilon_2)$ and $y_{C_2} = y_{C_1} + \sqrt{3} l_3 \sin(\alpha_1 + \varepsilon_1 + \varepsilon_2)$
280 where l_3 is the radius of the circle with center P_1 and passing through the passive revolute
281 joints at each vertex of the mobile platform, $\gamma_1 = 30°$ as the mobile platform corresponds
282 to an equilateral triangle.
283 In order to determine the inverse kinematic model (IKM) of the lower parallel mechanism,
284 the coordinates of point P_1 can be first expressed in the base reference frame R_0 such as:

$$\begin{cases} x_{P_1} = x_{A_i} + l_1 \cos(\alpha_i) + l_2 \cos(\beta_i) + l_3 \cos(\phi_z + \gamma_i) \\ y_{P_1} = y_{A_i} + l_1 \sin(\alpha_i) + l_2 \sin(\beta_i) + l_3 \sin(\phi_z + \gamma_i) \end{cases} \quad \text{for } i = 1, 2, 3 \quad (4)$$

285 where β_i is associated with the angular position of the first passive revolute joint of the i^{th}
286 serial chain, $\gamma_2 = \pi - \gamma_1$ and $\gamma_3 = -\frac{\pi}{2}$.
287 The angles β_i, then unknown, can be removed by calculating the expressions $\cos(\beta_i)$ and
288 $\sin(\beta_i)$, by squaring and summing the two equations of the previous system. The resulting
289 equation can then be written as $a \cos\alpha + b \sin\alpha - c = 0$, which gives:

$$\begin{aligned} &\left[2l_1 x_{A_i} - 2l_1 x_{P_1} + 2l_1 l_3 \, cos(\phi_z + \gamma_i)\right] cos(\alpha_i) \\ &\quad + \left[2l_1 y_{A_i} - 2l_1 y_{P_1} + 2l_1 l_3 \, sin(\phi_z + \gamma_i)\right] sin(\alpha_i) \\ &\quad + 2l_3 \, cos(\phi_z + \gamma_i)\left(x_{A_i} - x_{P_1}\right) + 2l_3 \, sin(\phi_z + \gamma_i)\left(y_{A_i} - y_{P_1}\right) \\ &\quad + {x_{P_1}}^2 + {x_{A_i}}^2 + {y_{P_1}}^2 + {y_{A_i}}^2 + {l_1}^2 - {l_2}^2 + {l_3}^2 - 2x_{P_1} x_{A_i} \\ &\quad - 2y_{P_1} y_{A_i} = 0 \end{aligned} \quad (5)$$

The expression of the joint positions of the three actuators of the lower parallel mechanism can thus be defined as follows:

$$\alpha_i = \text{atan2}(b_i, a_i) + \sigma_i \cos^{-1}\left(\frac{c_i}{\sqrt{{a_i}^2 + {b_i}^2}}\right) \quad \text{for } i = 1,2,3 \tag{6}$$

with $a_i = 2l_1x_{A_i} - 2l_1x_{P_1} + 2l_1l_3\cos(\phi_z + \gamma_i)$, $b_i = 2l_1y_{A_i} - 2l_1y_{P_1} + 2l_1l_3\sin(\phi_z + \gamma_i)$ and $c_i = -\left[2l_3\cos(\phi_z + \gamma_i)\left(x_{A_i} - x_{P_1}\right) + 2l_3\sin(\phi_z + \gamma_i)\left(y_{A_i} - y_{P_1}\right) + {x_{P_1}}^2 + {x_{A_i}}^2 + {y_{P_1}}^2 + {y_{A_i}}^2 + {l_1}^2 - {l_2}^2 + {l_3}^2 - 2x_{P_1}x_{A_i} - 2y_{P_1}y_{A_i}\right]$.

The IKM of the lower parallel mechanism has thus eight solutions, associated with the eight possible working modes of the 3-RRR mechanism. These modes depend on the sign of the coefficient σ_i (1 or -1) whose distribution is given in the following table for the three angles α_i:

Table 2 Possible working modes of the 3-RRR parallel mechanism

By deriving the IKM with respect to time, it is then possible to determine the parallel and serial Jacobian matrices, noted $\mathbf{A}_1$ and $\mathbf{B}_1$ respectively, such that:

$$\mathbf{B}_1\dot{\boldsymbol{\alpha}} = \mathbf{A}_1\dot{\mathbf{x}}$$

$$\begin{bmatrix} d_{11} & 0 & 0 \\ 0 & d_{12} & 0 \\ 0 & 0 & d_{13} \end{bmatrix}\begin{bmatrix} \dot{\alpha}_1 \\ \dot{\alpha}_2 \\ \dot{\alpha}_3 \end{bmatrix} = \begin{bmatrix} e_{11} & f_{11} & g_{11} \\ e_{12} & f_{12} & g_{12} \\ e_{13} & f_{13} & g_{13} \end{bmatrix}\begin{bmatrix} \dot{x}_{P_1} \\ \dot{y}_{P_1} \\ \dot{\phi}_z \end{bmatrix} \tag{7}$$

with $d_{1i} = -\big(-2l_1x_{A_i}\sin(\alpha_i) + 2l_1x_{P_1}\sin(\alpha_i) - 2l_1l_3\cos(\phi_z + \gamma_i)\sin(\alpha_i) + 2l_1y_{A_i}\cos(\alpha_i) - 2l_1y_{P_1}\cos(\alpha_i) + 2l_1l_3\sin(\phi_z + \gamma_i)\cos(\alpha_i)\big)$, $e_{1i} = -2l_1\cos(\alpha_i) - 2l_3\cos(\phi_z + \gamma_i) + 2x_{P_1} - 2x_{A_i}$, $f_{1i} = -2l_1\sin(\alpha_i) - 2l_3\sin(\phi_z + \gamma_i) + 2y_{P_1} - 2y_{A_i}$

and $g_{1i} = -2l_1 l_3 \sin(\phi_z + \gamma_i)\cos(\alpha_i) + 2l_1 l_3 \cos(\phi_z + \gamma_i)\sin(\alpha_i) - 2l_3 x_{A_i} \sin(\phi_z + \gamma_i) + 2l_3 x_{P_1} \sin(\phi_z + \gamma_i) + 2l_3 y_{A_i} \cos(\phi_z + \gamma_i) - 2l_3 y_{P_1} \cos(\phi_z + \gamma_i)$ for $i = 1, 2, 3$.

The Jacobian matrix of the lower parallel mechanism is thus written as:

$$\mathbf{J}_1 = (\mathbf{B}_1{}^{-1}\mathbf{A}_1)^{-1} \tag{8}$$

3.2.2. Upper parallel mechanism

Solving the DKM of the 3-RRR mechanism located at the upper part of the interface is simpler as it uses three identical serial chains to generate only two translational DoFs, resulting in one degree of redundancy. Three circle equations of center P_2 (see Fig. 8) and passing through the passive revolute joints B_i can therefore be define as:

$$\left(x_{P_2} - x_{B_i}\right)^2 + \left(y_{P_2} - y_{B_i}\right)^2 = {l_5}^2 \qquad \text{for } i = 4, 5, 6 \tag{9}$$

where l_5 represents the length of the second segment of each serial chain.

Fig. 8 Kinematic representation of the upper parallel mechanism

The coordinates of the end-effector of the upper parallel mechanism can thus be determined by rearranging the previous equations in matrix form such as:

$$\begin{bmatrix} x_{P_2} \\ y_{P_2} \end{bmatrix} = \begin{bmatrix} 2x_{B_4} - 2x_{B_5} & 2y_{B_4} - 2y_{B_5} \\ 2x_{B_4} - 2x_{B_6} & 2y_{B_4} - 2y_{B_6} \end{bmatrix}^{-1} \begin{bmatrix} {x_{B_4}}^2 + {y_{B_4}}^2 - {x_{B_5}}^2 - {y_{B_5}}^2 \\ {x_{B_4}}^2 + {y_{B_4}}^2 - {x_{B_6}}^2 - {y_{B_6}}^2 \end{bmatrix} \tag{10}$$

where $x_{B_i} = x_{A_i} + l_4 \cos(\alpha_i)$, $y_{B_i} = y_{A_i} + l_4 \sin(\alpha_i)$ for $i = 4{:}\,6$ and l_4 corresponds to the length of the first segment of each serial chain.

Concerning the IKM, the triangle $A_i B_i M$ is first considered in order to write the following equation:

$${l_5}^2 = {l_4}^2 + \left\|\overrightarrow{A_i P_2}\right\|^2 - 2l_4 \left\|\overrightarrow{A_i P_2}\right\| \cos(\alpha_i - \theta_i) \qquad \text{for } i = 4, 5, 6 \tag{11}$$

where θ_i corresponds to the angle between the $\vec{x}$ axis of the base reference frame R_O and the segment $[A_iP_2]$.

The expression of the joint positions of the three actuators of the upper parallel mechanism is thus:

$$\alpha_i = \text{atan2}\left(y_{P_2} - y_{A_i}, x_{P_2} - x_{A_i}\right) + \sigma_i \cos^{-1}\left(\frac{{l_5}^2 - {l_4}^2 - \left\|\overrightarrow{A_iP_2}\right\|^2}{2l_4\left\|\overrightarrow{A_iP_2}\right\|}\right) \text{ for } i = 4,5,6 \qquad (12)$$

As for the previous 3-RRR mechanism, there are eight IKM solutions depending on the sign of the coefficient σ_i (see Table 2), in other words, on the mechanism working mode.

The Jacobian matrix of this second mechanism is similar to the one obtained for the previous mechanism, with the terms associated with the rotation removed, such as:

$$\mathbf{B}_2\dot{\boldsymbol{\alpha}} = \mathbf{A}_2\dot{\mathbf{x}} \qquad (13)$$

$$\begin{bmatrix} d_{21} & 0 & 0 \\ 0 & d_{22} & 0 \\ 0 & 0 & d_{23} \end{bmatrix}\begin{bmatrix} \dot{\alpha}_1 \\ \dot{\alpha}_2 \\ \dot{\alpha}_3 \end{bmatrix} = \begin{bmatrix} e_{21} & f_{21} \\ e_{22} & f_{22} \\ e_{23} & f_{23} \end{bmatrix}\begin{bmatrix} \dot{x}_{P_2} \\ \dot{y}_{P_2} \end{bmatrix} \qquad (14)$$

with $d_i = -\left(-2l_4x_{A_i}\sin(\alpha_i) + 2l_4x_M\sin(\alpha_i) + 2l_4y_{A_i}\cos(\alpha_i) - 2l_4y_M\cos(\alpha_i)\right)$,

$e_i = -2l_4\cos(\alpha_i) + 2x_M - 2x_{A_i}$ and $f_i = -2l_4\sin(\alpha_i) + 2y_M - 2y_{A_i}$ for $i = 1,2,3$.

The Jacobian matrix of the lower parallel mechanism is thus obtained as follows:

$$\mathbf{J}_2 = (\mathbf{B}_2{}^{-1}\mathbf{A}_2)^{-1} \qquad (15)$$

3.2.3. Serial mechanism

Since the serial mechanism corresponds to an helical joint, the position of the end-effector in the end-effector reference frame R_e is calculated from the distance traveled by the nut along the threaded rod. Since the rotation of this rod is controlled by the seventh actuator, the position of the end-effector E can be expressed as follows:

$$z_{E/R_e} = \frac{p}{2\pi}\alpha_7 \tag{16}$$

where p corresponds to the thread pitch of the threaded rod.

The angular position of the seventh actuator is determined by inverting this last equation.

3.3. Direct and inverse kinematic models of the hybrid interface

The direct kinematic model of the hybrid interface is defined by the position and the orientation of the end-effector E (see Fig. 9). The operational vector $\mathbf{X} = \left[x_E\ y_E\ z_E\ \phi_x\ \phi_y\ \phi_z\right]^{\mathrm{T}}$ is obtained from the DKM of the three mechanisms previously presented such that:

$$\begin{cases} x_E = x_{P_1} + n_E.u_x \\ y_E = y_{P_1} + n_E.u_y \\ z_E = z_{P_1} + n_E.u_z \\ \phi_x = \mathrm{atan2}\left(z_{P_2} - z_{P_1}, y_{P_2} - y_{P_1}\right) \\ \phi_y = \mathrm{atan2}\left(z_{P_2} - z_{P_1}, x_{P_2} - x_{P_1}\right) \\ \phi_z \end{cases} \tag{17}$$

where $n_E = \left\|\overrightarrow{P_1P_2}\right\| - \left(d + z_{E/R_e}\right)$, d corresponds to the known and fixed distance between the point P_2 and the origin of the end-effector reference frame R_e, $u_x = \frac{x_{P_2} - x_{P_1}}{\left\|\overrightarrow{P_1P_2}\right\|}$, $u_y = \frac{y_{P_2} - y_{P_1}}{\left\|\overrightarrow{P_1P_2}\right\|}$, $u_z = \frac{z_{P_2} - z_{P_1}}{\left\|\overrightarrow{P_1P_2}\right\|}$ and the proper rotation ϕ_z is directly given by the DKM of the lower parallel mechanism.

Fig. 9 Kinematic representation of the hybrid interface

Concerning the IKM, the coordinates of the end-effectors of the parallel mechanisms can first be calculated knowing that:

$$\begin{cases}\phi_x = \text{atan2}\left(z_{P_2} - z_{P_1}, y_{P_2} - y_{P_1}\right) = \text{atan2}\left(z_{P_2} - z_E, y_{P_2} - y_E\right) = \text{atan2}\left(z_E - z_{P_1}, y_E - y_{P_1}\right) \\ \phi_y = \text{atan2}\left(z_{P_2} - z_{P_1}, x_{P_2} - x_{P_1}\right) = \text{atan2}\left(z_{P_2} - z_E, x_{P_2} - x_E\right) = \text{atan2}\left(z_E - z_{P_1}, x_E - x_{P_1}\right)\end{cases} \quad (18)$$

which gives:

$$\begin{cases} x_{P_2} = \dfrac{z_{P_2} - z_E}{\tan \phi_y} + x_E \\ y_{P_2} = \dfrac{z_{P_2} - z_E}{\tan \phi_x} + y_E \end{cases} \text{ and } \begin{cases} x_{P_1} = \dfrac{z_{P_1} - z_E}{\tan \phi_y} + x_E \\ y_{P_1} = \dfrac{z_{P_1} - z_E}{\tan \phi_x} + y_E \end{cases} \quad (19)$$

The position of the end-effector along the threaded rod can then be determined by calculating the coordinates of the origin of the end-effector reference frame R_e such that:

$$\mathbf{X}_e = \mathbf{X}_{P_1} + n_e \mathbf{u} \quad (20)$$

where $\mathbf{X}_e = [x_e \; y_e \; z_e]^{\mathrm{T}}$, $\mathbf{X}_{P_1} = \left[x_{P_1} \; y_{P_1} \; z_{P_1}\right]^{\mathrm{T}}$, $\mathbf{u} = \left[u_x \; u_y \; u_z\right]^{\mathrm{T}}$ and $n_e = \left\|\overrightarrow{P_1P_2}\right\| - d$.

The norm of the vector $\overrightarrow{eE}$ thus corresponds to the position z_{E/R_e} of the end-effector.

Knowing these parameters, the IKM of the complete hybrid interface can thus be obtained using the IKM of each mechanism presented previously, as shown in figure 10.

Fig. 10 Block diagram of the IKM for the complete hybrid interface

3.4. Choice of working modes

As mentioned before, the two parallel mechanisms each have 8 different working modes, resulting in 64 possible working modes for the interface. In order to choose the appropriate working modes for both parallel mechanisms, an analysis of the dexterity distribution within the workspace of the two mechanisms was carried out.

Dexterity is an index that measures the distance of mechanism from a singularity, i.e. a configuration in which the mechanism loses or gains a degree of freedom and therefore becomes uncontrollable.

One of the most widely used methods of calculating dexterity is based on the condition number of the Jacobian matrix [47,48], defined as:

$$\kappa = \|\mathbf{J}\|.\|\mathbf{J}^{-1}\| \tag{21}$$

where $\|\mathbf{J}\|$ is the invariant Euclidean norm of the matrix $\mathbf{J}$.

However, the matrix $\mathbf{J}_1$ of the lower parallel mechanism is non-homogeneous since it has terms associated with the position and orientation of the end-effector P_1. This is not the case with matrix $\mathbf{J}_2$, which is only associated with the position of the end-effector P_2. Before calculating the condition number of matrix $\mathbf{J}_1$, the last column of the parallel matrix $\mathbf{A}_1$ must thus be divided by a characteristic length L defined according to the orientation of the mobile platform such that:

$$\begin{cases} L = \sqrt{2}\, l_3 \sin(\phi_z) & \text{if } \phi_z \neq 0 + k\pi \\ L = \sqrt{2}\, l_3 & \text{else} \end{cases} \tag{22}$$

The condition number varies between 1 and $\propto$ and dexterity, denoted η, is determined as:

$$\eta = \frac{1}{\kappa} \tag{23}$$

The dexterity is then between 0 and 1. A dexterity close to 0 corresponding to a singular configuration of the mechanism.

Figures 11 and 12 show the distribution of dexterity on the workspace of two 3-RRR mechanisms, with and without a moving platform respectively, depending on the working mode. To display these results, the two parallel mechanisms were built with a distance of 200 mm between the active revolute joints, the lengths l_1 and l_2 of the legs of each serial

chain are equal to 60 mm and 100 mm respectively and the mobile platform of the first mechanism has a radius of 20 mm.

For the lower parallel mechanism (see Fig. 11), modes 1 and 8 show maximum dexterity achieved at the center of the mechanism's workspace. Also, unlike the other modes, the high dexterity zone is located around the same central point. The singularities are therefore closer to the boundaries of the workspace than for the other working modes. The same observations can also be made for the upper parallel mechanism (see Fig. 12). At this stage, working modes 1 and 8 have been selected. The final choice between these two modes is made later, based on which will minimize the motor torques according to the desired force feedback.

Fig. 11 Distribution of dexterity over the entire workspace of the lower parallel mechanism as a function of the working mode

Fig. 12 Distribution of dexterity over the entire workspace of the lower parallel mechanism as a function of the working mode

4. INPUT FORCES AND ACTIVE JOINT TORQUES RELATIONSHIP

As mentioned in section 2.2, in the context of teleoperated robotic cervical surgery, it is essential to provide force feedback to the surgeon during each drilling to avoid any risk of undesirable perforation of the bone. In addition, force feedback can be used to create virtual walls to ensure that the interface end-effector remains within the prescribed workspace associated with the task. Moreover, the weight of the interface moving parts can be taken into account to enable gravitational compensation. Consequently, the interface can adjust

to counterbalance gravitational forces and maintain its balance, without needing the operator's involvement.

In order to enable the interface to provide the desired forces, a relationship has been established between the desired force vector and vector of the torques generated by the interface's active joints. For simplification purposes, the weight of the interface's moving parts has been neglected. Therefore, gravitational compensation of the interface is not implemented in this work.

Knowing the desired force feedback vector $\mathbf{F}_{des} = \left[F_{des_x}\ F_{des_y}\ F_{des_z}\ \mathcal{M}_{des_x}\ \mathcal{M}_{des_y}\ \mathcal{M}_{des_z}\right]$ and the direction of the forces that can be exerted by the parallel and serial mechanisms of the interface, it is possible to determine the torque τ_i that each of the seven motors of the interface must generate.

In fact, the parallel mechanisms can only exert forces in the plane $(\vec{x}, \vec{y})$, and the serial mechanism can only generate a force along the central axis of the interface connecting points P_1 and P_2, i.e. the end-effectors of the upper and lower parallel mechanisms respectively (see Fig. 13).

Fig. 13 Representation of the forces exerted by the parallel and serial mechanisms of the interface

The force vectors exerted by each mechanism expressed in the interface reference frame are thus noted as follow:

$$\begin{cases} \mathbf{F}_{P_1} = \left[F_{P_{1x}} \quad F_{P_{1y}} \quad 0 \quad 0 \quad 0 \quad \mathcal{M}_{P_{1z}}\right]^{\mathrm{T}} \\ \mathbf{F}_{P_2} = \left[F_{P_{2x}} \quad F_{P_{2y}} \quad 0 \quad 0 \quad 0 \quad 0\right]^{\mathrm{T}} \\ \mathbf{F}_S = \left[F_{S_x} \quad F_{S_y} \quad F_{S_z} \quad 0 \quad 0 \quad 0\right]^{\mathrm{T}} \end{cases} \tag{24}$$

where $\mathbf{F}_S$ corresponds to the force exerted by the serial mechanism.

445 Firstly, given that the serial mechanism is the only one capable of generating forces along
446 the $\vec{z}$ axis of the interface reference frame, the z-axis component of the force $\mathbf{F}_S$ can be
447 expressed as:

$$F_{S_z} = F_{des_z} \tag{25}$$

448 In addition, the components of the force exerted by the serial mechanism can be written as:

$$\mathbf{F}_S = n_u \mathbf{u} \tag{26}$$

449 where $\mathbf{F}_S = \left[F_{S_x}\, F_{S_y}\, F_{S_z}\right]^{\mathrm{T}}$, $\mathbf{u} = \left[u_x\, u_y\, u_z\right]^{\mathrm{T}}$, $u_x = \frac{x_{P_2} - x_{P_1}}{\|\overrightarrow{P_1P_2}\|}$, $u_y = \frac{y_{P_2} - y_{P_1}}{\|\overrightarrow{P_1P_2}\|}$ and $u_z =$
450 $\frac{z_{P_2} - z_{P_1}}{\|\overrightarrow{P_1P_2}\|}$ are the components of the unit vector of the force $\mathbf{F}_S$ and x_{P_i}, y_{P_i} and z_{P_i} are the
451 coordinates of the points P_i known from the direct kinematic model of the parallel
452 mechanisms presented previously.
453 The value of the coefficient n_u is then determined from the knowledge of the components
454 F_{S_z}, such as:

$$n_u = \frac{F_{S_z}}{u_z} = \frac{F_{des_z}}{u_z} \tag{27}$$

455 The components along the $\vec{x}$ and $\vec{y}$ axes can then be calculated as:

$$F_{S_x} = \frac{F_{des_z}}{u_z} \times u_x \quad \text{and} \quad F_{S_y} = \frac{F_{des_z}}{u_z} \times u_y \tag{28}$$

456 In the end-effector reference frame R_e, we note:

$$\mathbf{F}_{S_{/R_e}} = \begin{bmatrix} 0 & 0 & F_{S_{z_{/R_e}}} \end{bmatrix}^{\mathrm{T}} \tag{29}$$

457 where $F_{S_{z_{/R_e}}} = \left\|\mathbf{F}_{S_{/R_e}}\right\| = \|\mathbf{F}_S\| = \sqrt{{F_{S_x}}^2 + {F_{S_y}}^2 + {F_{S_z}}^2}$.

458 Knowing the thread pitch p of the threaded rod of the serial mechanism, the torque to be
459 applied is defined as follows:

$$\tau_7 = \frac{p}{2\pi} \times F_{S_{z/R_e}} \tag{30}$$

460 Subsequently, the forces that must be exerted by the parallel mechanisms along the $\vec{x}$ and

461 $\vec{y}$ axes of the interface can be determined:

$$\mathbf{F}_{P_1} + \mathbf{F}_{P_2} + \mathbf{F}_S = \mathbf{F}_{des} = \begin{bmatrix} F_{des_x} & F_{des_y} \end{bmatrix}^{\mathrm{T}} \tag{31}$$

$$\boldsymbol{\mathcal{M}}_E(\mathbf{F}_{P_1}) + \boldsymbol{\mathcal{M}}_E(\mathbf{F}_{P_2}) + \boldsymbol{\mathcal{M}}_E(\mathbf{F}_S) = \boldsymbol{\mathcal{M}}_{des} = \begin{bmatrix} \mathcal{M}_{des_x} & \mathcal{M}_{des_y} \end{bmatrix}^{\mathrm{T}} \tag{32}$$

462 Equation (32) gives:

$$\begin{cases} \mathcal{M}_{des_x} = \left(\overrightarrow{EP_1} \wedge \mathbf{F}_{P_1}\right)_x + \left(\overrightarrow{EP_2} \wedge \mathbf{F}_{P_2}\right)_x = -z_{EP_1} F_{P_{1_y}} - z_{EP_2} F_{P_{2_y}} \\ \mathcal{M}_{des_y} = \left(\overrightarrow{EP_1} \wedge \mathbf{F}_{P_1}\right)_y + \left(\overrightarrow{EP_2} \wedge \mathbf{F}_{P_2}\right)_y = z_{EP_1} F_{P_{1_x}} + z_{EP_2} F_{P_{2_x}} \end{cases} \tag{33}$$

463 where $\left(\overrightarrow{EP_1} \wedge \mathbf{F}_{P_1}\right)_x$ corresponds to the x-axis component of the vector product and z_{EP_i} is

464 the component of vector $\overrightarrow{EP_i}$ along the $\vec{z}$ axis.

465 The components of the force $\mathbf{F}_{P_1}$ can then be written as follows:

$$\begin{cases} F_{P_{1_x}} = \dfrac{\mathcal{M}_{des_y} - z_{EP_2} F_{P_{2_x}}}{z_{EP_1}} \\ F_{P_{1_y}} = \dfrac{-\mathcal{M}_{des_x} - z_{EP_2} F_{P_{2_y}}}{z_{EP_1}} \end{cases} \tag{34}$$

466 Replacing $F_{P_{1_x}}$ and $F_{P_{1_y}}$ in equation (31) gives:

$$\begin{cases} F_{P_{2_x}} = \dfrac{z_{EP_1}}{z_{EP_1} - z_{EP_2}} \left(F_{des_x} - F_{S_x} - \dfrac{\mathcal{M}_{des_y}}{z_{EP_1}} \right) \\ F_{P_{2_y}} = \dfrac{z_{EP_1}}{z_{EP_1} - z_{EP_2}} \left(F_{des_y} - F_{S_y} + \dfrac{\mathcal{M}_{des_x}}{z_{EP_1}} \right) \end{cases} \tag{35}$$

467 At this stage, it remains to determine the moment to be exerted by the lower mechanism

468 around the $\vec{z}$ axis in order to generate the desired moment and to compensate for the

469 moments caused by the forces applied by the two parallel mechanisms. Thus, we note:

$$\begin{aligned}\mathcal{M}_{P_{1_z}} &= \mathcal{M}_{des_z} - \left(\overrightarrow{\boldsymbol{EP}_1} \wedge \mathbf{F}_{P_1}\right)_z - \left(\overrightarrow{\boldsymbol{EP}_2} \wedge \mathbf{F}_{P_2}\right)_z \\ &= \mathcal{M}_{des_z} - \left(x_{EP_1} F_{P_{1_y}} - y_{EP_1} F_{P_{1_x}} + x_{EP_2} F_{P_{2_y}} - y_{EP_2} F_{P_{2_x}}\right)\end{aligned} \tag{36}$$

Knowing the Jacobian matrices $\mathbf{J}_1$ and $\mathbf{J}_2$, derived from the kinematic models of the parallel mechanisms, the torques of each actuator, numbered from 1 to 3 for the lower mechanism and from 4 to 6 for the upper mechanism, can be calculated such that:

$$\begin{cases}\boldsymbol{\tau}_{1,2,3} = \mathbf{J}_1{}^{\mathrm{T}}.\mathbf{F}_{P_1} = \mathbf{J}_1{}^{\mathrm{T}}\begin{bmatrix}F_{P_{1_x}} & F_{P_{1_y}} & \mathcal{M}_{P_{1_z}}\end{bmatrix}^{\mathrm{T}} \\ \boldsymbol{\tau}_{4,5,6} = \mathbf{J}_2{}^{\mathrm{T}}.\mathbf{F}_{P_2} = \mathbf{J}_2{}^{\mathrm{T}}\begin{bmatrix}F_{P_{2_x}} & F_{P_{2_y}}\end{bmatrix}^{\mathrm{T}}\end{cases} \tag{37}$$

In summary, the torques to be provided by each actuator are calculated as follows:

$$\begin{cases}\boldsymbol{\tau}_{1,2,3} = \mathbf{J}_1{}^{\mathrm{T}}\begin{bmatrix}F_{des_x} - F_{P_{2_x}} - F_{S_x} \\ F_{des_y} - F_{P_{2_y}} - F_{S_y} \\ \mathcal{M}_{des_z} - \left(x_{EP_1} F_{P_{1_y}} - y_{EP_1} F_{P_{1_x}} + x_{EP_2} F_{P_{2_y}} - y_{EP_2} F_{P_{2_x}}\right)\end{bmatrix} \\ \boldsymbol{\tau}_{4,5,6} = \mathbf{J}_2{}^{\mathrm{T}}\begin{bmatrix}\dfrac{z_{EP_1}}{z_{EP_1} - z_{EP_2}}\left(F_{des_x} - F_{S_x} - \dfrac{\mathcal{M}_{des_y}}{z_{EP_1}}\right) \\ \dfrac{z_{EP_1}}{z_{EP_1} - z_{EP_2}}\left(F_{des_y} - F_{S_y} - \dfrac{\mathcal{M}_{des_x}}{z_{EP_1}}\right)\end{bmatrix} \\ \tau_7 = \dfrac{p}{2\pi} \times F_{S_{z/R_e}}\end{cases} \tag{38}$$

5. INTERFACE OPTIMIZATION AND DESIGN

5.1. Optimization problem formulation

Knowing the specifications that the interface needed to meet in terms of workspace and force feedback, the interface was then optimized. The aim of this optimization is to find the optimal geometric parameters of the interface, defined within a design vector **I**, to satisfy a set of criteria and constraints associated with an objective function noted $f(\mathbf{I})$. Once this objective function was defined, an optimization algorithm was used: the genetic algorithm (GA) available in Matlab's *Optimization* toolbox. The GA iteratively searches

for the optimal design vector that minimizes the function $f(\mathbf{I})$. Between each iteration, the algorithm chooses a new design vector to evaluate according to the value interval $[v_{inf} \;\; v_{max}]$ chosen for each design variable (i.e. geometric parameter), so that the optimal solution found belongs to the search interval defined beforehand.

The design vector $\mathbf{I}$ is thus composed of seven parameters. Firstly, it contains the x_a parameter, which defines the position of the actuators of the parallel mechanisms of the interface. Secondly, the parameter z_m associated with the distance between the parallel mechanisms, i.e. the dimension of the serial mechanism. Finally, the lengths l_i which correspond to the dimensions of the legs and mobile platform of the parallel mechanisms (see Fig. 14).

$$\mathbf{I} = [x_a \;\; z_m \;\; l_1 \;\; l_2 \;\; l_3 \;\; l_4 \;\; l_5] \tag{39}$$

Fig. 14 Representation of the geometric parameters of the interface

Three criteria are considered for the optimization problem, namely maximizing the minimum dexterity of the two parallel mechanisms in order to avoid any singularity inside the workspace, minimizing the motor torques required to generate the desired force feedback, and minimizing the interface volume. These three criteria, respectively noted $\mathrm{f}_1(\mathbf{I})$, $\mathrm{f}_2(\mathbf{I})$ and $\mathrm{f}_3(\mathbf{I})$, are formulated as follows:

$$\mathrm{f}_1(\mathbf{I}) = 1 - \eta_{min} \tag{40}$$

$$\mathrm{f}_2(\mathbf{I}) = \frac{1}{7n_p} \sum_{i=1}^{7} \sum_{j=1}^{n_p} \left(\frac{|\tau_{i,j}|}{\tau_{max_i}} \right) \tag{41}$$

$$\mathrm{f}_3(\mathbf{I}) = \frac{V_{interface}}{V_{max}} \tag{42}$$

where η_{min} is the average of the minimum dexterities of the parallel mechanisms, n_p is the number of poses constituting the prescribed workspace, $\tau_{i,j}$ is the torque provided by actuator i associated with pose j of the prescribed workspace, τ_{max_i} is the maximum torque that can be generated by actuator i, $V_{interface}$ is the volume occupied by the interface calculated from the parameters x_a and z_m, and V_{max} corresponds to the maximum volume of the interface that can be obtained from the maximum values chosen for the search intervals of the parameters x_a and z_m. The three criteria $\mathrm{f}_i(\mathbf{I})$ are thus defined to be between 0 and 1. A value close to 0 being associated with high minimum dexterity, low motor torques and minimal interface volume.

In addition, a constraint on the prescribed workspace must considered to ensure that the interface can reach any desired end-effector pose. A minimum level of dexterity is also required to ensure that the interface does not encounter a singularity at any of the coordinates of the prescribed workspace. A third constraint relates to the motor torque distribution criterion, which must be between the limit values τ_{max_i} and τ_{min_i}, in order to guarantee the desired force feedback.

A penalty formulation of the optimization problem is considered to handle the previous constraints. Three penalty functions, denoted p_1, p_2 and p_3, have been defined in order to reject undesirable individuals, i.e. design vectors incompatible with the established constraints.

Thus, the objective function $\mathrm{f}(\mathbf{I})$ can be formulated as the sum of the weighted average of the three criteria f_1, f_2 and f_3 and the three penalties p_1, p_2 and p_3 associated respectively

524 with constraints on the workspace, dexterity and the distribution of motor torques such
525 that:

$$\mathrm{f}(\mathbf{I}) = \beta_1.\mathrm{f}_1(\mathbf{I}) + \beta_2.\mathrm{f}_2(\mathbf{I}) + \beta_3.\mathrm{f}_3(\mathbf{I}) + \sum_j \left(p_{1_j} + p_{2_j} + p_{3_j}\right) \quad \text{for } j = 1,..,n_p \tag{43}$$

526 with:

$$p_{1_j} = \begin{cases} 0 & \text{if } \mathbf{P}_j \in \text{interface workspace} \\ \lambda_1 & \text{if } \mathbf{P}_j \notin \text{one of the three mechanisms workspace} \\ 2\lambda_1 & if\ \mathbf{P}_j \notin \text{two of the three mechanisms workspaces} \\ 3\lambda_1 & \text{else} \end{cases} \tag{44}$$

$$p_{2_j} = \begin{cases} 0 & \text{if } \eta_{min\,sup_j} \geq 0.15 \text{ and } \eta_{min\,inf_j} \geq 0.15 \\ \lambda_2 & \text{else} \end{cases} \tag{45}$$

$$p_{3_j} = \begin{cases} 0 & \text{if } \max\left(\tau_{i,j}\right)_i \leq \tau_{max_m} \text{ and } \min\left(\tau_{i,j}\right)_i \geq \tau_{min_m} \\ \lambda_3 & \text{else} \end{cases} \tag{46}$$

527 where β_1, β_2 and β_3 are the weight coefficients of the three criterion functions, n_p is the
528 number of poses composing the prescribed workspace, $\eta_{min\,sup_j}$ is the minimum dexterity
529 of the upper parallel mechanism associated with the pose $\mathbf{P}_j\left(x_j, y_j, z_j, \phi_{x_j}, \phi_{y_j}, \phi_{z_j}\right)$ of the
530 end-effector, $\eta_{min\,inf_j}$ is the minimum dexterity of the lower parallel mechanism, and λ_1,
531 λ_2 and λ_3 are large-valued scalars.
532 The bounding values, in millimeters, chosen for the design variables are as follows:

$$\begin{aligned} v_{inf} &= [250\ \ 200\ \ 100\ \ 150\ \ 20\ \ 100\ \ 150] \\ v_{max} &= [350\ \ 300\ \ 200\ \ 250\ \ 30\ \ 200\ \ 250] \end{aligned} \tag{47}$$

533
534 **5.2. Optimization results**
535
536 The optimal design vector, denoted $\mathbf{I}^*$ and in millimeters, as a result of the optimization
537 problem, is obtained by choosing the weighting coefficients $\beta_1 = 0.5$, $\beta_2 = \beta_3 = 0.25$ to

favor the maximization of the minimum dexterity over the minimization of the interface volume.

$$\mathbf{I}^{*} = [320.9\ 245.6\ 140.7\ 196.8\ 30.0\ 171.3\ 187.5] \quad (48)$$

The minimal dexterity value within the prescribed workspace for the lower parallel mechanism and for the upper parallel mechanism is equal to 0.17 and 0.19 respectively.

5.2.1. Interface workspace

The workspace of the optimized interface is determined from the IKMs previously established. As shown in figure 15, two types of workspace can be distinguished: a translational workspace where the orientation of the end-effector is kept fixed; and a rotational workspace where the initial position of the end-effector is fixed and the end-effector scans the possible range of rotation as well as all the accessible positions along the $\vec{z}$ axis of the end-effector. The translational workspace is thus linked to the tool positioning phase at the desired drilling entry point (see Fig. 3a). While the rotational workspace is associated with drilling execution, i.e. the prescribed cone-shaped workspace (see Fig. 3b and 3c).

Figure 15a shows the translational workspace obtained when the end-effector is held vertically and for an orientation of 90° of the mobile platform of the lower parallel mechanism. In addition, figure 15b shows two rotational workspaces constructed from two different initial positions of the interface end-effector.

Fig. 15 (a) Translational workspace with fixed end-effector orientation equal to 90° *and (b) rotational workspaces of the interface around the drilling entry point with coordinates* [160.5 92.6 100] *mm in blue and* [125 175 90] *mm in orange*

5.2.2. Motor torque distribution

The torques to be generated by each actuator were computed over the entire prescribed workspace. Figure 16 shows the results obtained for a desired force feedback vector $\mathbf{F}_{des} = [10 \ -10 \ 30 \ -0.5 \ -0.5 \ 0.5]$ N and N.m corresponding to the critical force feedback generating the highest torques. The torque values for each actuator for the configurations with the highest and lowest dexterity values for the two parallel mechanisms are shown with green and red lines respectively. The corresponding configurations are shown on figures 16a and 16b.

Fig. 16 Distribution of motor torques generated by each actuator for the configurations where the dexterity values of the parallel mechanisms are (a) the highest and (b) the lowest

These results were obtained by selecting working mode 1 for the two parallel mechanisms since it minimised the motor torques required for the same force feedback compared with working mode 8.

5.3. Design of a motorized prototype

Following the optimization, a motorized prototype of the interface was designed taking into account the optimal geometric dimensions obtained (see Fig. 17).

For actuation, Simplex SC040 servomotors will be used for the parallel mechanisms and a Simplex SE010 servomotor will be used to control the serial mechanism of the interface [49]. Knowing the maximum torques that these servomotors can provide, 0.8 N.m and 0.4 N.m respectively, capstans were added to the design for the parallel mechanisms so that the interface can generate the desired force feedback (see Fig. 16). The output torque of the actuators of the parallel mechanisms will thus be multiplied by the ratio of the diameter of

the capstan to the diameter of the driving pulley, fixed on the axis of the considered actuator.

Since the motor 1 of the lower parallel mechanism must provide a maximum torque of 6.2 N.m in order to ensure the desired force feedback associated with the drilling task, a radius of 80.5 mm was chosen for the capstans of the lower mechanism. The radius of the drive pulleys being 9.45 mm, the reduction ratio is thus approximately equal to 8.5.

For the upper parallel mechanism, a maximum torque of 0.9 N is achieved for motor 5. A reduction ratio of 1.125 would therefore be sufficient to enable the motor to deliver the required torque. However, for manufacture reasons, the upper capstans have been oversized by choosing a radius of 40 mm, giving a reduction ratio of approximately 4.2.

Concerning the serial mechanism, the maximum torque that the motor can deliver is much higher than the maximum torque required, validating the choice of the motor. In addition, a threaded rod with a diameter of 5 mm and a thread pitch equal to 10 mm was chosen in order to generate a reversible translation of the nut linked to the end-effector of the interface.

Finally, since the main disadvantage of hybrid mechanisms is friction, ball bearings and self-lubricating bronze bushings are used to cope with this issue. Tight dimensional and geometric tolerances also contribute to minimize friction.

Fig. 17 Design of the motorized interface prototype

6. CONCLUSION AND FUTURE WORK

This paper presented a 6-DoF hybrid interface dedicated to teleoperated cervical spine surgery. The proposed architecture consists of two parallel mechanisms controlling the position and orientation of a central rod on which a serial mechanism is mounted to control linear translation. In the context of posterior cervical arthrodesis, the association of the parallel and serial mechanisms will allow to fix the CoR as well as the orientation of the central rod, linked to the entry point and the orientation of the drilling. In addition, the serial mechanism, which can be decoupled from the other mechanisms, will control the drilling tool advance along the selected drilling axis, thus meeting the expectations of the cervical drilling task. In addition to the geometry of the surgical task, coupled with the definition of the prescribed workspace covered by the interface, realistic force feedback must be provided to the surgeon to identify in which bone zone the drilling is taking place, cortical or cancellous, thus avoiding any undesirable perforation of the bone.

After solving the direct and inverse kinematic models of the entire hybrid interface and establishing the relationship between input forces and active joint torques, the design parameters of the interface were optimized within three criteria. The first criterion was the dexterity distribution within the prescribed workspace to avoid singularities. The second criterion was the motor torques distribution with the aim of minimization. Finally, the final objective was to reduce the interface volume. After obtaining the optimal design vector, a motorized prototype was designed.

Future work will consist of assembling this prototype and implementing its control. This task should allow, on the one hand, the retrieval of the end-effector pose from the interface, which will then be sent as a setpoint to a robot, and, on the other hand, the generation of force feedback at the interface, which will be associated with the interaction forces exerted

between the robot and the external environment. This will lead to an experimental validation of the interface through the control of a robotic arm in a teleoperation scheme.

ACKNOWLEDGMENT

This work was supported by the University of Poitiers and by the CNRS through the International Research Project *RACeS*.

FUNDING

- University of Poitiers
- CNRS, the French National Centre for Scientific Research, through the International Research Project RACeS (Robotic Assisted System for Safe Cervical Surgery) (TWN-IRP-17).[2]

[2] https://irp-races.prd.fr/

650 **NOMENCLATURE**
651

$(x,y)_{A_i}$	coordinates of points A_i corresponding to the active revolute joints of the parallel mechanisms
$(x,y)_{B_i}$	coordinates of point B_i corresponding to the first passive revolute joints of the parallel mechanisms
$(x,y)_{C_i}$	coordinates of point C_i corresponding to the vertex of the mobile platform of the lower parallel mechanism
$(x,y)_{P_1}$	coordinates of the end-effector P_1 of the lower parallel mechanism
$(x,y)_{P_2}$	coordinates of the end-effector P_2 of the upper parallel mechanism
$\mathbf{X}$	operational vector resulting from the DKM of the interface
$(x,y,z)_E$	coordinates of the end-effector E of the serial mechanism and the interface
$\phi_{(x,y,z)}$	orientation of the end-effector of the interface
l_1	length of the first legs of the serial branches of the lower parallel mechanism
l_2	length of the second legs of the serial branches of the lower parallel mechanism
l_3	radius of the mobile platform
l_4	length of the first legs of the serial branches of the upper parallel mechanism

l_5 length of the second legs of the serial branches of the upper parallel mechanism

α_i joint position of the actuator i of the interface

ε_i angle provide by the sensor i

γ_i angle locating the vertex i of the mobile platform

θ_i angle between the $\vec{x}$ axis of the base reference frame R_O and the segment $[A_i\ P_2]$ of the upper parallel mechanism

σ_i coefficient equal to 1 or -1 depending on the working mode of the 3-RRR mechanism

$(\dot{x}, \dot{y})_{P_1}$ Cartesian velocities of the end-effector P_1 of the lower parallel mechanism

$\dot{\phi}_z$ rotation velocity of the mobile platform

$\mathbf{A}_1$ parallel Jacobian matrix of the lower parallel mechanism

$\mathbf{B}_1$ serial Jacobian matrix of the lower parallel mechanism

$\mathbf{J}_1$ Jacobian matrix of the lower parallel mechanism

$(\dot{x}, \dot{y})_{P_2}$ Cartesian velocities of the end-effector P_2 of the upper parallel mechanism

$\mathbf{A}_2$ parallel Jacobian matrix of the upper parallel mechanism

$\mathbf{B}_2$ serial Jacobian matrix of the upper parallel mechanism

$\mathbf{J}_2$ Jacobian matrix of the upper parallel mechanism

z_{E/R_e}	position of the end-effector of the serial mechanism in the end-effector reference frame R_e
p	thread pitch of the threaded rod of the serial mechanism
d	distance between the point P_2 and the origin of the end-effector reference frame R_e
n_E	distance between the point P_1 and the end-effector E of the interface
$u_{(x,y,z)}$	components of the direction vector of the segment $[P_1\ P_2]$
n_e	distance between the point P_1 and the origin e of the end-effector reference frame R_e
κ	condition number of the Jacobian matrix
η	dexterity index
$\mathbf{F}_{des}$	desired force feedback vector
$F_{des_{(x,y,z)}}$	components of the desired force
$\mathcal{M}_{des_{(x,y,z)}}$	components of the desired moments
τ_i	torque generated by the actuator i of the interface
$\mathbf{F}_{P_1}$	force vector exerted by the lower parallel mechanism
$F_{P_{1(x,y)}}$	components of the force exerted by the lower parallel mechanism
$\mathcal{M}_{P_{1z}}$	components of the moment exerted by the lower parallel mechanism
$\mathbf{F}_{P_2}$	force vector exerted by the upper parallel mechanism

$F_{P_{2(x,y)}}$	components of the force exerted by the upper parallel mechanism
$\mathbf{F}_S$	force vector exerted by the serial mechanism
$F_{S_{(x,y,z)}}$	components of the force exerted by the serial mechanism
n_u	coefficient of proportionality between the component of the force $\mathbf{F}_S$ and the component of the direction vector of the segment $[P_1\ P_2]$
$\mathbf{F}_{S_{/R_e}}$	force vector exerted by the serial mechanism expressed in the end-effector reference frame R_e
$\boldsymbol{\mathcal{M}}_E(\mathbf{F})$	moment of a force $\mathbf{F}$ about point E
$(x,y,z)_{EP_i}$	components of vector $\overrightarrow{EP_i}$
$\mathbf{I}$	design vector of the interface
x_a	parameter associated with the position of the actuators of the parallel mechanism of the interface
z_m	distance between the parallel mechanisms
$\mathrm{f}_i(\mathbf{I})$	criterion function i for optimization
η_{min}	average of the minimum dexterities of the parallel mechanisms
n_p	number of poses constituting the prescribed workspace
$\tau_{i,j}$	torque provided by actuator i associated with pose j of the prescribed workspace
τ_{max_i}	maximum torque that can be generated by actuator i
$V_{interface}$	volume occupied by the interface

V_{max}	maximum volume of the interface obtained from the maximum values chosen for the parameters x_a and z_m
β_i	weight coefficients of the three criterion functions
p_i	penalty i associated with constraints on the workspace, dexterity and the distribution of motor torques
v_{inf}	minimum bounding values for the design variables
v_{max}	maximum bounding values for the design variables
$\mathbf{I}^*$	optimal design vector of the interface

652

REFERENCES

[1] Farooq Usmani, M., Gopinath, R., Camacho, J. E., Gentry, R., and Ludwig, S. C., 2020, "Management of cranio-cervical injuries: C1-C2 posterior cervical fusion and decompression," Seminars in Spine Surgery, **32**(1). DOI: 10.1016/j.semss.2019.100782

[2] Molliqaj, G, Paun, L., Nouri, A., Girod, P.-P., Schaller, K., and Tessitore, E., 2020, "Role of robotics in improving surgical outcome in spinal pathologies," World Neurosurgery **140**, pp. 664-673. DOI: 10.1016/j.wneu.2020.05.132

[3] Avrumova, F., Sivaganesan, A., Alluri, R. K., Vaishnav, A., Qureshi, S., and Lebl, D. R., 2021, "Work-flow and efficiency of robotic-assisted navigation in spine surgery," HSS J. **17**(3), pp. 302-307. DOI: 10.1177/15563316211026658

[4] Koszulinski, A., Sandoval, J., Vendeuvre, T., Zeghloul, S., and Laribi, M. A., 2022, "Comanipulation Robotic Platform for Spine Surgery with Exteroceptive Visual Coupling: Development and Experimentation," ASME Journal of Medical Devices, **16**(4), pp. 041002_1-11. DOI: 10.1115/1.4054550

[5] Koszulinski, A., Sandoval, J., and Laribi, M. A., 2023, "Design and modelisation of a 6 degrees of freedom interface with repositionable centre of rotation. New Advances in Mechanisms, Transmissions and Applications," *MeTrApp 2023, Mechanisms and Machine Science*, eds., Springer, Cham, **124**, pp. 286-296. DOI: 10.1007/978-3-031-29815-8_28

[6] Ewerton, M., Rother, D., Weimar, J., Kollegger, G., Wiemeyer, J., Peters, J., and Maeda, G., 2018, "Assisting Movement Training and Execution With Visual and Haptic Device," Frontiers in Neurorobotics, **12**, pp. 12-24. DOI: 10.3389/fnbot.2018.00024

[7] Rhienmora, P., Haddawy, P., Dailey, M., Khanal, P., and Suebnukarn, S., 2008, "Development of a Dental Skills Training Simulator Using Virtual Reality and Haptic Device," NECTEC Technical Journal, **8**(20), pp. 140-147. DOI:

[8] Gautreau, E., Sandoval, J., Thomas, A., Guilhem, J.-M., Carbone, G., Zeghloul, S., and Laribi, M. A., 2022, "Redundancy Exploitation of an 8-DoF Robotic Assistant for Doppler Sonography," Actuators, **11**(2), pp. 33. DOI: 10.3390/act11020033

[9] Abeywardena, S., and Chen, C., 2017, "Implementation and evaluation of a three-legged six-degrees-of-freedom parallel mechanism as an impedance-type haptic device," IEEE/ASME Transactions on Mechatronics, **22**(3), pp. 1412-1422. DOI: 10.1109/TMECH.2017.2682930

[10] Meskini, M., Saafi, H., Mlika, A., Arsicault, M., Zeghloul, S., and Laribi, M. A., 2023, "Development of a novel hybrid haptic (nHH) device with a remote center of rotation

dedicated to laparoscopic surgery," Robotica, **41**(10), pp. 3175-3194. DOI: 10.1017/S0263574723000942

[11] Goel, A., Desai, K. I., and Muzumdar, D., P., 2002, "Atlantoaxial fixation using plate and screw method: a report of 160 treated patients, " Neurosurgery, **51**(6), pp. 1351-1357. DOI: 10.1227/01.NEU.0000035852.23082.C6

[12] Simsek, S., Yigitkanli, K., Seçkin, H., Comert, A., Acar, H. I., Belen, D., Tekdemir, I., and Elhan, A., 2009, "Ideal screw entry point and projection angles for posterior lateral mass fixation of the atlas: an anatomical study," European Spine Journal, **18**(9), pp. 1321-1325. DOI: 10.1007/s00586-009-1105-7

[13] Merola, A. A., Castro, B. A., Alongi, P. R, Mathur, S., Brkaric, M., Vigna, F., Riina, J. P., Gorup, J., and Haher, T., 2002, "Anatomic consideration for standard and modified techniques of cercial lateral mass screw placement," The spine journal: official journal of the North American Spine Society, **2**(6), pp. 430-435. DOI: 10.1016/S1529-9430(02)00461-8

[14] Abdullah, K. G., Nowacki, A. S., Steinmetz, M. P., Wang, J. C., and Mroz, T. E., 2011, "Factors affecting lateral mass screw placement at C-7: Clinical article," Journal of neurosurgery, Spine, **14**(3), pp. 405-411. DOI: 10.3171/2010.11.SPINE09776

[15] Ebraheim, N. A., Treamins, M. R., Xu, R., and Yeasting, R. A., 1998, "Lateral radiologic evaluation of lateral mass screw placement in the cervical spine," Spine, **23**(4), pp. 458-462. DOI: 10.1097/00007632-199802150-00010

[16] Xu, R., Ebraheim, N. A., Klausner, T., and Yeasting, R. A., 1998, "Modified Magerl technique of lateral mass screw placement in the lower cervical spine: an anatomic study," Journal of Spinal Disorders, **11**(3), pp. 237-240. DOI: 10.1097/00002517-199806000-00011

[17] Liu, G., Xu, R., Ma, W., Sun, S., and Feng, J., 2011, "Anatomical considerations for the placement of cervical transarticular screws: Laboratory investigation," Journal of neurosurgery, Spine, **14**(1), pp. 114-121. DOI: 10.3171/2010.9.SPINE1066

[18] Senoglu, M., Safavi-Abbasi, S., Theodore, N., Crawford, N. R., and Sonntag, V. K. H., 2010, "Feasible and accurate occipitoatlantal transarticular fixation: an anatomic study," Neurosurgery, **66**(3), pp. 173-177. DOI: 10.1227/01.NEU.0000350982.03929.05

[20] Xu, R., Zhao, L., Chai, B., Ma, W., Xia, H., Wang, G., and Jiang, W., 2009, "Lateral radiological evaluation of transarticular screw placement in the lower cervical spine," European Spine Journal, **18**(3), pp. 392-397. DOI: 10.1007/s00586-008-0861-0

[21] Lee, K. M., Yeom, J. S., Lee, J. O., Buchowski, J. M., Park, K.-W., Chang, B.-S., Lee, C.-K., and Riew, K. D., 2010, "Optimal trajectory for the atlantooccipital transarticular screw," Spine, **35**(16), pp. 1562-1570. DOI: 10.1097/BRS.0b013e3181c15a84

[22] Zhao, L., Xu, R., Liu, J., Sochacki, K. R., Ma, W., Jiang, W., Liu, G., Cao, J., and Hua, Q., 2012, "The study on comparison of 3 techniques for transarticular screw placement in the lower cervical spine," Spine, **37**(8), pp. 468-472. DOI: 10.1097/BRS.0b013e318237aae4

[23] Cassinelli, E. H., Lee, M., Skalak, A., Ahn, N. U., and Wright, N. M., 2006, "Anatomic considerations for the placement of C2 laminar screws," Spine, **31**(24), pp. 2767-2771. DOI: 10.1097/01.brs.0000245869.85276.f4

[24] Ma, X.-Y., Yin, Q.-S., Wu, Z.-H., Xia, H., Riew, K. D., and Liu, J.-F., 2010, "C2 anatomy and dimensions relative to translaminar screw placement in an Asian population," Spine, **35**(6), pp. 704-708. DOI: 10.1097/BRS.0b013e3181bb8831

[25] Saetia, K., and Phankhongsab, A., 2014, "C2 anatomy for translaminar screw placement based on computerized tomographic measurements," Asian Spine Journal, **9**(2), pp. 205-209. DOI: 10.4184/asj.2015.9.2.205

[26] Wang, M. Y., 2006, "C2 crossing laminar screws: cadaveric morphometric analysis," Neurosurgery, **59**(1), pp. 84-88. DOI: 10.1227/01.NEU.0000219900.24467.32

[27] Ji, W., Liu, X., Huang, W., Huang, Z., Li, X., Chen, J., Wu, Z., and Zhu, Q., 2015, "Feasibility of C2 Vertebra Screws Placement in Patient With Occipitalization of Atlas: A Tomographic Study," Medicine, **94**(7), pp. 1492. DOI: 10.1097/MD.0000000000001492

[28] Yue, B., Kwak, D.-S., Kim, M.-K., Kwon, S.-O., and Han, S.-H., 2010, "Morphometric trajectory analysis for the C2 crossing laminar screw technique," European Spine Journal, **19**(5), pp. 828-832. DOI: 10.1007/s00586-010-1331-z

[29] Kong, G., Ji, W., Huang, Z., Liu, J., Chan, J., and Zhu, Q., 2017, "The risk of translaminar screw fixation to the transverse foramen of the lower cervical spine: a computed tomography study," Scientific Reports, **7**(1), pp. 46611. DOI: 10.1038/srep46611

[30] Tan, K.-A., Lin, S., Chin, B. Z., Thadani, V. N., Hey, H. W. D., 2020, "Anatomic techniques for cervical pedicle screw placement," Journal of Spine Surgery, **6**(1), pp. 262-273. DOI: 10.21037/jss.2020.03.07

[31] Faghih-Jouibari, M., Moazzeni, K., Amini-Navai, A., Hanaei, S., Abdollahzadeh, S., and Khanmohammadi, R., 2016, "Anatomical considerations for insertion of pedicular screw in cervicothoracic junction," Iranian Journal of Neurosurgery, **15**(4), pp. 228-231.

[32] Abumi, K., 2015, "Cervical spondylotic myelopathy: posterior decompression and pedicle screw fixation," European Spine Journal, **24**(2), pp. 186-196. DOI: 10.1007/s00586-015-3838-9

[33] Abumi, K., Itoh, H., Taneichi, H., and Kaneda, K., 1994, "Transpedicular screw fixation for traumatic lesions of the middle and lower cervical spine," Journal of Spinal Disorders, **7**(1), pp. 19-28. DOI: 10.1097/00002517-199407010-00003

[34] Yoon, S.-D., Lee, J. Y., Lee, I-S., Moon, S. M., Cho, B. M., Park, S.-H., and Oh, S.-M., 2013, "Cervical pedicle screw placement in sawbone models and unstable cervical traumatic lesions by using para-articular mini-laminotomy: a novice neurosurgeon's experience," Korean Journal of Neurotrauma, **9**(2), pp. 106-113. DOI: 10.13004/kjnt.2013.9.2.106

[35] Panjabi, M. M., Duranceau, J., Goel, V., Oxland, T., and Takata, K., 1990, "Cervical human vertebrae quantitative three-dimensional anatomy of the middle and lower regions," Spine, **16**(8), pp. 861-869. DOI: 10.1097/00007632-199108000-00001

[36] Richter, M., Cakir, B., Schmidt, R., 2005, "Cervical pedicle screws: conventional versus computer-assisted placement of cannulated screws," Spine, **30**(20), pp. 2280-2287. DOI: 10.1097/01.brs.0000182275.31425.cd

[37] Tian, W., Han, X., Liu, B., Liu, Y., Hu, Y., Han, X., Xu, Y., Fan, M., and Jin, H., 2013, "A robot-assisted surgical system using a force-image control method for pedicle screw insertion," PLoS ONE, **9**(1). DOI: 10.1371/journal.pone.0086346

[38] Wolf, A., Shoham, M., Michael, S., and Moshe, R., 2004, "Feasibility study of a mini, bone-attached, robotic system for spinal operations," Spine, **29**(2), pp. 220-228. DOI: 10.1097/01.BRS.0000107222.84732.DD

[39] Matsumiya, K., Momoi, Y., Kobayashi, E., Sugano, N., Yonenobu, K., Inada, H., Tsuji, T., and Sakuma, I., 2003, "Forces and torques during robotic needle insertion to human vertebra," International Congress Series, **1256**, pp. 492-497. DOI: 10.1016/S0531-5131(03)00472-2

[40] Wolf, A., Shoham, M., Michael, S., and Moshe, R., 2001, "Morphometric study of the human lumbar spine for operation-workspace specifications," Spine, **26**(22), pp. 2472-2477. DOI: 10.1097/00007632-200111150-00015

[41] Rezazadeh, S., Bai, W., Sun, M., Chan, S., Lin, Y., and Cao, Q., 2019, "Robotic spinal surgery system with force feedback for teleoperated drilling," The Journal of Engineering, **2019**(14), pp. 500-505. DOI: 10.1049/joe.2018.9407

[42] Jin, H., Hu, Y., Tian, W., Zhang, P., Zhang, J., and Li, B., 2014, "Safety analysis and control of a robotic spinal surgical system," Mechatronics, **24**(1), pp. 55-65. DOI: 10.1016/j.mechatronics.2013.11.008

[43] Hu, Y., Jin, H., Zhang, L., Zhang, P., Zhang, J., 2014, "State recognition of pedicle drilling with force sensing in a robotic spinal surgical system," IEEE/ASME Transactions of Mechatronics, **19**(1), pp. 357-365. DOI: 10.1109/TMECH.2012.2237179

[44] Powers, M. J., 2006, "The mechanics of bone drilling: experiment and finite element predictions," Ph.D. thesis, University of Calgary, Calgary, Alberta, Canada.

[45] Gosselin, C. M., Sefrioui, J., and Richard, M. J., 1992, "Solutions polynomiales au problème de la cinématique directe des manipulateurs parallèles plans à trois degrés de liberté," Mechanism and Machine Theory, **27**(2), pp. 107-119. DOI: 10.1016/0094-114X(92)90001-X

[46] Merlet, J.-P., 1993, "Algebraic-Geometry Tools for the Study of Kinematics of Parallel Manipulators," Computational Kinematics, **28**, pp. 183-194. DOI: 10.1007/978-94-015-8192-9_17

[47] Alba-Gomez, O., Wenger, P., and Pamanes, 2005, "Consistent Kinetostatic Indices for Planar3-DOF Parallel Manipulators, Application to the Optimal Kinematic Inversion," *Proceedings of the ASME 2005 International Design Engineering Technical Conferences and Computers and Information in Engineering Conference*. Volume 7: 29th Mechanisms and Robotics Conference, Parts A and B, **7**, pp. 765-774. DOI: 10.1115/DETC2005-84326

[48] Quintero-Riaza, H. F., Mejía-Calderón, L. A., and Díaz-Rodríguez, M., 2019, "Synthesis of planar parallel manipulators including dexterity, force transmission and stiffness index," Mechanics Based Design of Structures and Machines, **47**(6), pp. 680-702. DOI:10.1080/15397734.2019.1615503

[49] Simplex motion, Integrated Servomotors, https://simplexmotion.com/integrated-servomotors/se-series/, last access 15/10/2023

859 **Figure Captions List**
860

Fig. 1 Illustration of posterior cervical arthrodesis

Fig. 2 (a) Virtuose 6D by Haption, (b) Omega 3 parallel interface by Force Dimension, (C) MEPaM developed by Abeywardena *et al.* and (d) Hybrid interface developed by Meskini *et al.*

Fig. 3 Illustration of the drilling procedure and the prescribed workspaces

Fig. 4 Summary of the results of the literature review conducted on the drilling parameters of five different drilling gestures

Fig. 5 (a) Typical curve of the evolution of the force applied along the drilling axis and (b) histograms of the maximum values of force and moment found in the literature

Fig. 6 Representation of the interface architecture and the degrees of freedom obtain with each mechanism: (a) the upper mechanism, (b) the lower mechanism, (c) the assembly of the two parallel mechanisms and (d) the serial mechanism

Fig. 7 Kinematic representation of (a) the lower parallel mechanism and (b) its mobile platform

Fig. 8 Kinematic representation of the upper parallel mechanism

Fig. 9 Kinematic representation of the hybrid interface

Fig. 10 Block diagram of the IKM for the complete hybrid interface

Fig. 11 Distribution of dexterity over the entire workspace of the lower parallel mechanism as a function of the working mode

Fig.12 Distribution of dexterity over the entire workspace of the lower parallel mechanism as a function of the working mode

Fig. 13 Representation of the forces exerted by the parallel and serial mechanisms of the interface

Fig. 14 Representation of the geometric parameters of the interface

Fig. 15 (a) Translational workspace with fixed end-effector orientation equal to 90° and (b) rotational workspaces of the interface around the drilling entry point with coordinates $[160.5\ 92.6\ 100]$ mm in blue and $[125\ 175\ 90]$ mm in orange

Fig. 16 Distribution of motor torques generated by each actuator for the configurations where the dexterity values of the parallel mechanisms are (a) the highest and (b) the lowest

Fig. 17 Design of the motorized interface prototype

861
862

863 **Table Caption List**
864

Table 1 Main advantages and disadvantages of the rigid-link interface classes

Table 2 Possible working modes of the 3-RRR parallel mechanism

865
866

867 **Figure 1: Illustration of posterior cervical arthrodesis**
868

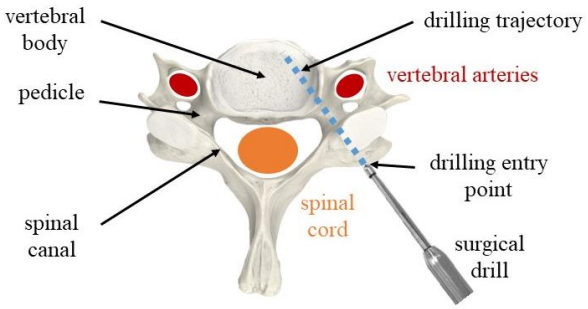

869
870

Figure 2: (a) Virtuose 6D by Haption, (b) Omega 3 parallel interface by Force Dimension, (C) MEPaM developed by Abeywardena *et al.* and (d) Hybrid interface developed by Meskini *et al.*

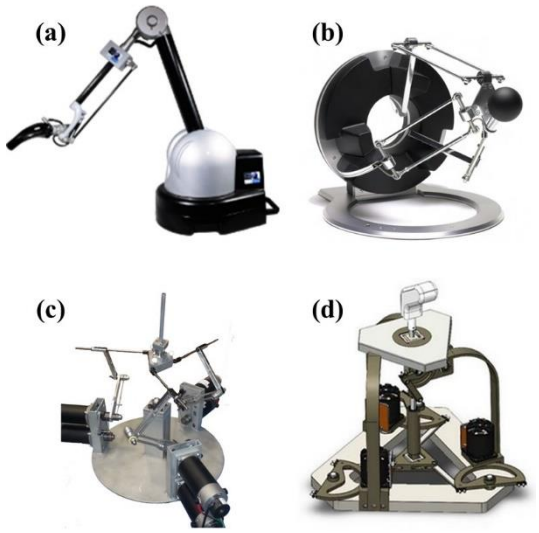

878 **Figure 3: Illustration of the drilling procedure and the prescribed workspaces**
879

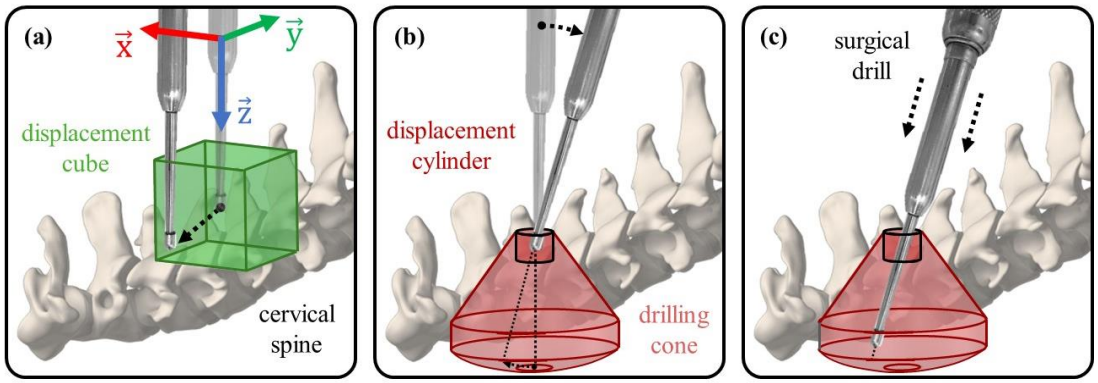

880
881

Figure 4: Summary of the results of the literature review conducted on the drilling parameters of five different drilling gestures

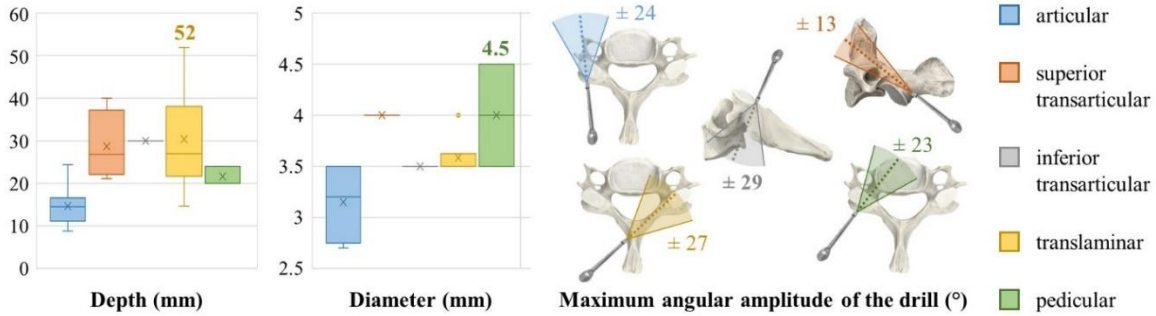

887 **Figure 5: (a) Typical curve of the evolution of the force applied along the drilling axis**
888 **and (b) histograms of the maximum values of force and moment found in the**
889 **literature**
890

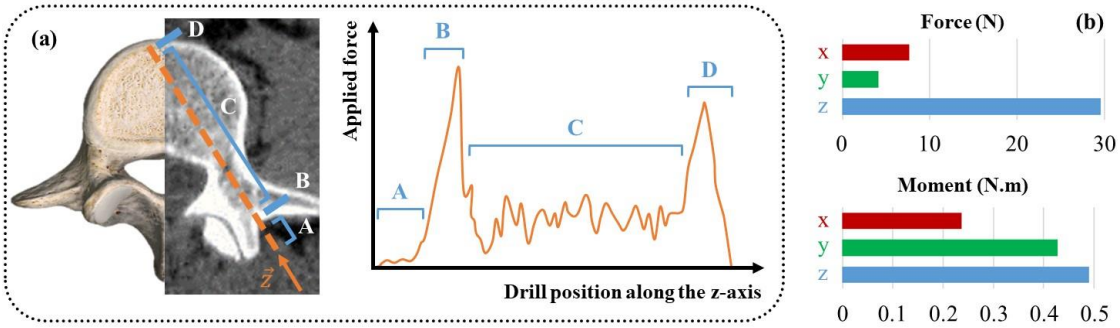

891
892

Figure 6: Representation of the interface architecture and the degrees of freedom obtain with each mechanism: (a) the upper mechanism, (b) the lower mechanism, (c) the assembly of the two parallel mechanisms and (d) the serial mechanism

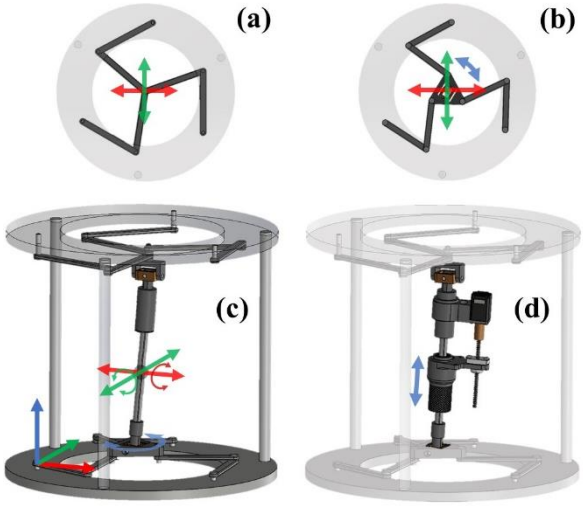

899 **Figure 7: Kinematic representation of (a) the lower parallel mechanism and (b) its**
900 **mobile platform**
901

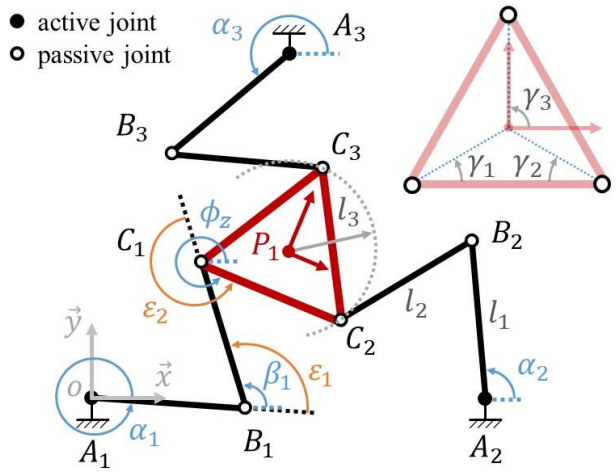

902
903

Figure 8: Kinematic representation of the upper parallel mechanism

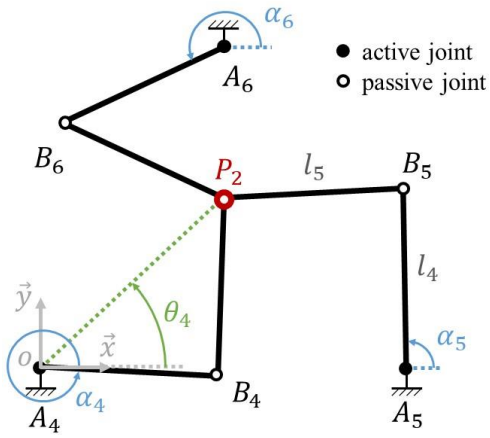

908 **Figure 9: Kinematic representation of the hybrid interface**
909

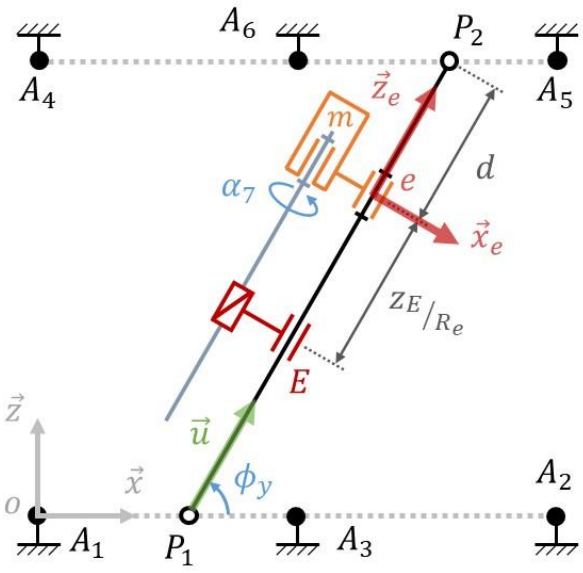

910
911

912 **Figure 10: Block diagram of the IKM for the complete hybrid interface**
913

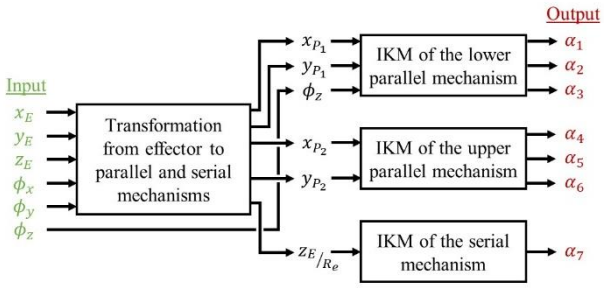

914
915

Figure 11: Distribution of dexterity over the entire workspace of the lower parallel mechanism as a function of the working mode

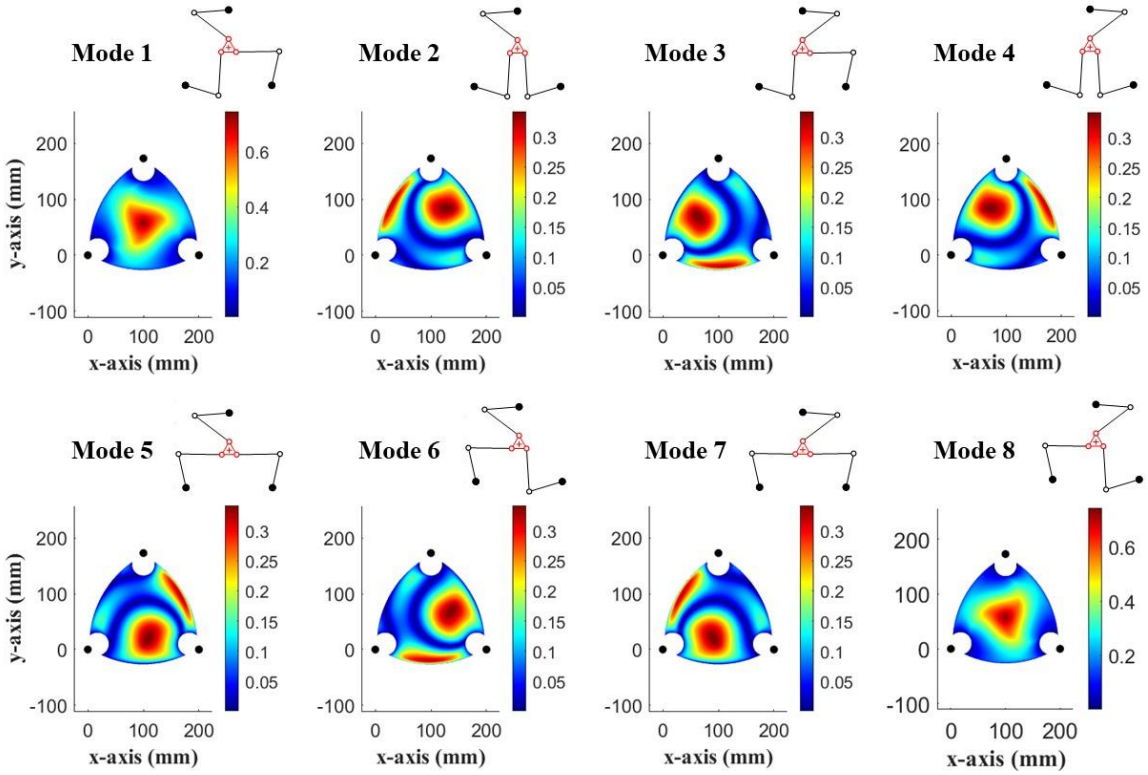

Figure 12: Distribution of dexterity over the entire workspace of the lower parallel mechanism as a function of the working mode

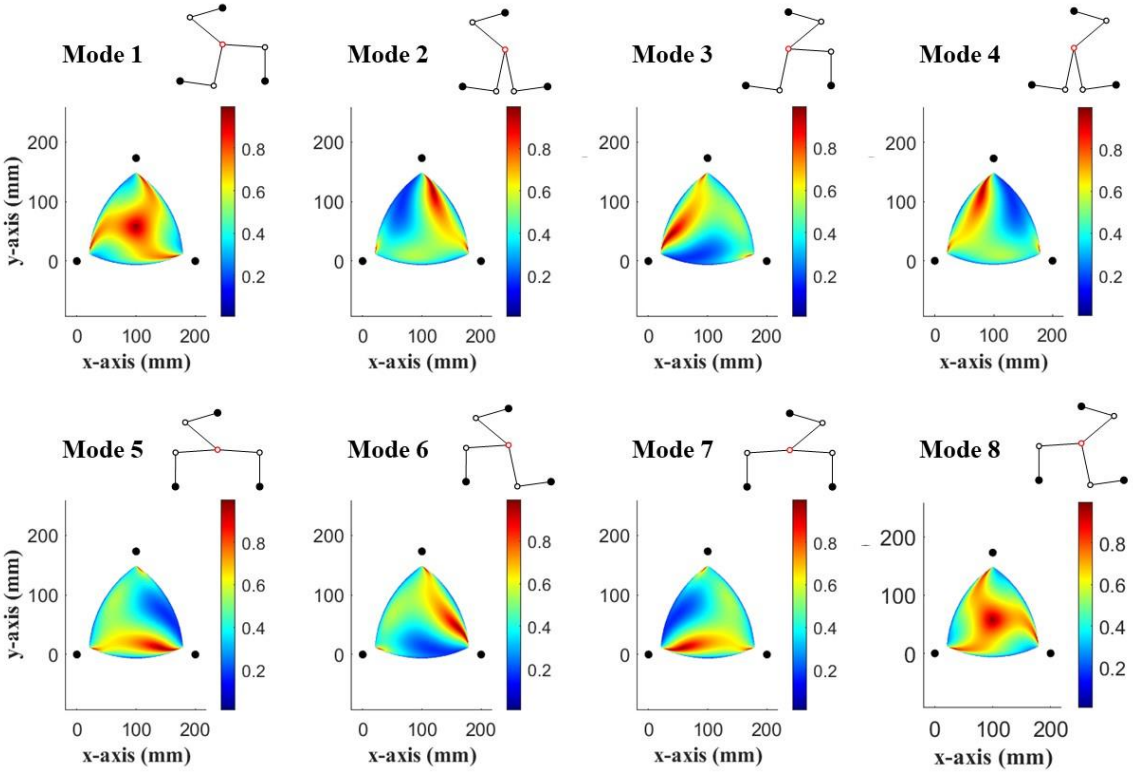

926 **Figure 13: Representation of the forces exerted by the parallel and serial mechanisms**
927 **of the interface**
928

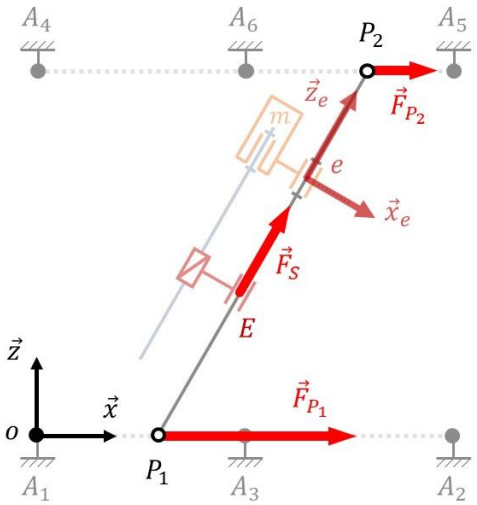

929
930

931 **Figure 14: Representation of the geometric parameters of the interface**
932

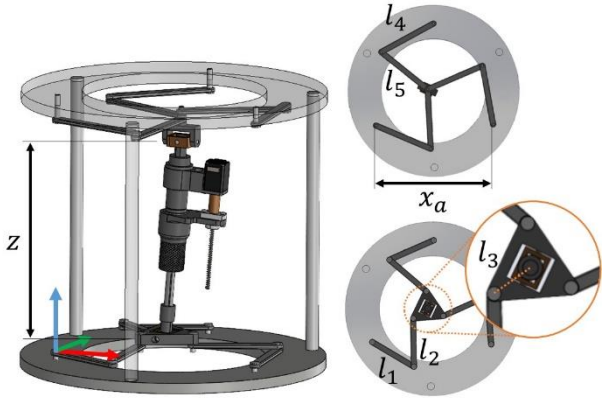

933
934

Figure 15: (a) Translational workspace with fixed end-effector orientation equal to 90° and (b) rotational workspaces of the interface around the drilling entry point with coordinates [160.5 92.6 100] mm in blue and [125 175 90] mm in orange

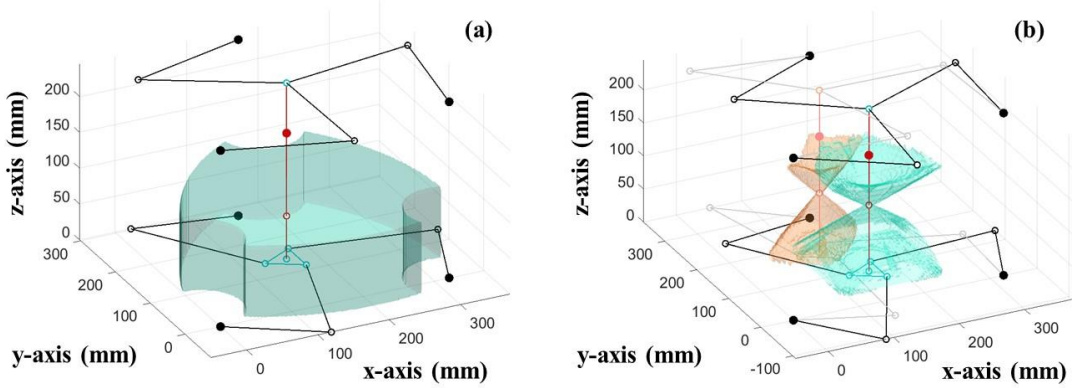

941 **Figure 16: Distribution of motor torques generated by each actuator for the**
942 **configurations where the dexterity values of the parallel mechanisms are (a) the**
943 **highest and (b) the lowest**
944

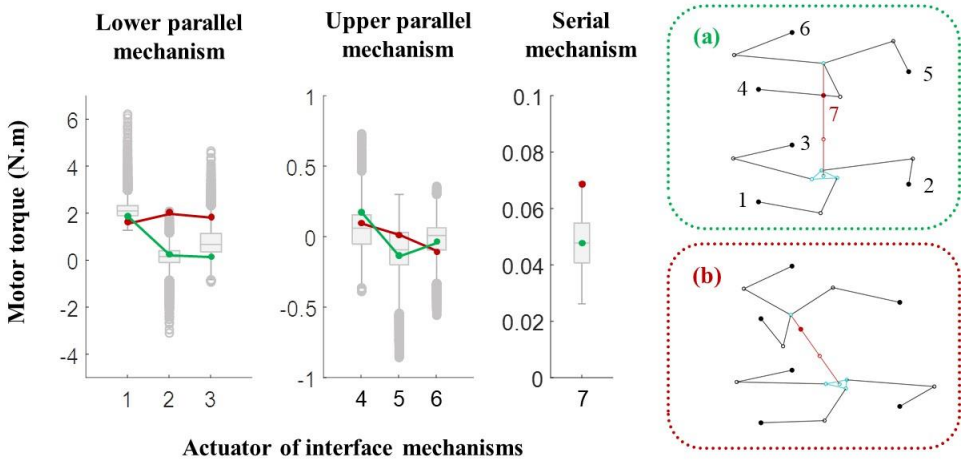

945
946

947 **Figure 17: Design of the motorized interface prototype**
948

949
950

951 **Table 1: Main advantages and disadvantages of the rigid-link interface classes**
952

Class	Advantages	Disadvantages
Serial	• Large workspace	• Need for more powerful actuators • Low rigidity • Lower accuracy • Higher inertia
Parallel	• High rigidity • Increased accuracy	• Limited workspace • Higher friction • Low compactness
Hybrid	• Combines the advantages of serial and parallel classes	• Low compactness • Friction

953

954 **Table 2: Possible working modes of the 3-RRR parallel mechanism**
955

Mode	1	2	3	4	5	6	7	8
σ_1	+	+	+	+	-	-	-	-
σ_2	+	-	+	-	+	-	+	-
σ_3	+	+	-	-	+	+	-	-

956